Geophys. Astrophys. Fluid Dynamics, Vol. 43, pp. 181–222
Reprints available directly from the publisher
Photocopying permitted by license only
© 1988 Gordon and Breach, Science Publishers, Inc.
Printed in Great Britain

Finite Amplitude Holmboe Waves

W. D. SMYTH, G. P. KLAASSEN and W. R. PELTIER*

Department of Physics, University of Toronto, Toronto, Ontario, Canada M5S 1A7

(*Received 13 October 1987; in final form 22 February 1988*)

We investigate the evolution of a parallel shear flow which has embedded within it a thin, symmetrically positioned layer of stable density stratification. The primary instability of this flow may deliver either Kelvin–Helmholtz waves or Holmboe waves, depending on the strength of the stratification. In this paper we describe a sequence of numerical simulations which reveal for the first time the behavior of the Holmboe wave at finite amplitude and clarify its structural relationship to the Kelvin–Helmholtz wave.

The flows investigated have initial profiles of horizontal velocity and Brunt–Vaisala frequency given in nondimensional form by $U=\tanh\zeta$ and $N^2=J\,\mathrm{sech}^2 R\zeta$, respectively, in which ζ is a nondimensional vertical coordinate, J is the value of the gradient Richardson number $N^2/(dU/d\zeta)^2$ at $\zeta=0$, and $R=3$. Linear stability theory predicts that the flow will develop Holmboe instability when J exceeds some critical value J_c, and Kelvin–Helmholtz instability when J is less than J_c; J_c being approximately equal to 0.25 when $R=3$. We simulate the evolution of flows with $J=0.9$, $J=0.45$, and $J=0.22$, and find that the first two simulations yield Holmboe waves while the third yields a Kelvin–Helmholtz wave, as predicted.

The Holmboe wave is a superposition of two oppositely propagating disturbances, a right-going mode whose energy is concentrated in the region above the centre of the shear layer, and a left-going mode whose energy is concentrated below the centre of the shear layer. The horizontal speed of the modes varies periodically, and the variations are most pronounced at low values of J. If $J\leqq J_c$, the minimum horizontal speed of the modes vanishes and the modes become phase-locked, whereupon they roll up to form a Kelvin–Helmholtz wave as predicted by Holmboe (1962). When J is moderately greater than J_c, the Holmboe wave ejects long, thin plumes of fluid into the regions above and below the shear layer, as has often been observed in laboratory experiments, and we examine in detail the mechanism by which this occurs.

KEY WORDS: Shear flows, stability, stratified fluids.

*John Simon Guggenheim Foundation Fellow.

1. INTRODUCTION

It is generally accepted that a laminar flow may become turbulent via a finite sequence of supercritical transitions, each of which introduces a new element of complexity into the flow. Transition occurs when the magnitude of some control parameter exceeds a value beyond which the current flow state loses stability. First proposed by Ruelle and Takens (1971), this scenario for the transition to turbulence is most strikingly evident in the Bénard problem, in which a fluid layer heated from below exhibits a sequence of increasingly complex yet individually distinctive patterns of flow as the temperature difference between its upper and lower boundaries is increased. Since there is no corresponding external energy source in the free shear flow problem, the parameter which controls the transitions must be connected with the flow itself, most likely with the amplitude of the instantaneous wave state. The primary and higher-order instabilities of the Bénard flow have been identified and studied extensively [e.g., the review by Busse (1981)]; the effort to catalogue in similar fashion the instabilities of the free shear layer is at a relatively primitive stage, due largely to the greater complexity of the initial flows in which the secondary and higher-order transitions appear (Thorpe, 1987). Attention has been focussed almost exclusively on the Kelvin–Helmholtz wave and the secondary instabilities to which it succumbs at large amplitude (Patnaik *et al.*, 1976; Peltier *et al.* 1978; Corcos and Sherman, 1984; Corcos and Lin, 1984; Klaassen and Peltier, 1985a, b, c).

However, the Kelvin–Helmholtz wave is not the only primary instability of a stratified shear layer. Holmboe (1962) showed, in particular, that if the stratification takes the form of a sharp change in density at the centre of the shear layer, then the flow may exhibit either the Kelvin–Helmholtz instability or a related oscillatory instability, depending on the magnitude of the density jump. The finite-amplitude manifestation of the oscillatory instability is now referred to as the Holmboe wave (Browand and Wang, 1972). The importance of Holmboe waves in geophysical flows has yet to be established. They are liable to be less common than Kelvin–Helmholtz waves, since they occur under more restricted conditions. Structures resembling Holmboe waves have appeared in photographs (Spedding, 1988) and radar observations (e.g. Emmanuel *et al.*, 1972;

Gossard and Richter, 1970) of the atmosphere, but positive identification of these disturbances as Holmboe waves from a single "snapshot" is impossible due to the time-dependence of the waveform. In addition, information regarding the expected form of a large amplitude Holmboe waves in geophysical flows is sparse. Holmboe waves have been observed frequently in the laboratory (Keulegan, 1949; Ellison and Turner, 1959 [see description in Townsend (1958, p. 372)]; Thorpe, 1968a; Browand and Wang, 1972; Browand and Winant, 1973; Koop, 1976; Yoshida, 1977; Koop and Browand, 1979; Maxworthy and Browand, 1975; Tritton and Davies, 1985; Lawrence *et al.*, 1987), but theoretical results from beyond the linear regime have not existed before now. In this paper we present the results of a sequence of numerical simulations of shear layers enclosing abrupt density changes of various magnitudes. The results of these numerical experiments reveal the behavior of the Holmboe wave as it grows to large amplitude, and clarify its relationship to the Kelvin–Helmholtz wave.

We begin in Section 2 with a discussion of the linear theory, summarizing and extending the inviscid analyses of Hazel (1972). We then consider the effects of viscosity and heat conduction on the mean flow and on the growth rates of the instabilities, and conclude the section with a discussion of the dimensionality of the primary Holmboe instability. Section 3 is devoted to a discussion of the methodology employed in the simulations: the numerical model used to evolve the fields, the initial conditions chosen, and the diagnostic analyses employed to interpret the results. In Section 4, the results of the nonlinear simulations are presented and discussed. We describe a sequence of flow simulations which spans the parameter space from the Holmboe to the Kelvin–Helmholtz regime. A summary of the results is given in Section 5.

All of our analyses in the present paper will focus upon the symmetric case, in which the shear, the buoyancy frequency, and the boundary conditions are symmetric with respect to the centre of the shear layer. This is a highly idealized special case which is not likely to occur in nature, but it is the simplest context in which to study the essential dynamics of the wave. The effects of asymmetry in the profiles or boundary conditions will be explored in a separate paper. Future investigations will also include detailed analysis of the secondary instabilities to which the primary nonlinear Holmboe wave is subject.

2. LINEAR THEORY

In this section we shall first describe the stability properties of the stably stratified shear layer, using a normal-mode formulation for an inviscid, vertically unbounded flow. We then briefly discuss the effects of diffusion and of symmetrically placed upper and lower boundaries on the evolution of the flow. Finally, we consider the dimensionality of the Holmboe instability, i.e. whether or not the fastest-growing primary instability is necessarily two-dimensional.

The flows to be discussed here evolve from initial conditions of stably stratified parallel shear flow in which the horizontal and vertical components of velocity and the potential temperature have the following mathematical forms:

$$u_1 = u_0 \tanh(z/h). \quad u_3 = 0, \quad \theta = \Theta \exp[\Delta \tanh(Rz/h)], \tag{1}$$

in which u_0 and Δ are constants and Θ is a constant reference value for the potential temperature. The domain extends vertically from $z = -\infty$ to $z = +\infty$. The half-depths of the shear layer and the inversion are h and h/R respectively. A two-layer model is obtained in the limit as $R \to \infty$. (It will be shown below that setting $R = 3$ is sufficient to introduce effects characteristic of a two-layer flow, i.e. the appearance of Holmboe instability when the stratification is sufficiently strong.) Note that the potential temperature profile is nearly identical to a tanh profile provided that $\Delta \ll 1$. The "exp-tanh" version is employed here for analytical convenience, as it yields a simple form for the logarithmic derivative of θ, which appears in the definitions of the buoyancy frequency and the gradient Richardson number.

The inviscid Boussinesq equations for an ideal gas are

$$\begin{aligned} Du_i/Dt &= -\bar{\rho}^{-1} \partial p/\partial x_i + \theta^* g \delta_{i3}, \\ D\theta^*/Dt &= 0, \quad \partial u_j/\partial x_j = 0, \end{aligned} \tag{2}$$

in which $\bar{\rho}$ is a constant reference density and

$$\theta^* \equiv (\theta - \Theta)/\Theta \simeq -(\rho - \bar{\rho})/\bar{\rho},$$

provided that departures of θ and ρ from their respective reference values are small. When these equations are linearized about the

steady state solution (1) and the appropriate boundary conditions applied, the result is a boundary value problem for the perturbation fields with independent variables x, z, and t. The usual approach to this problem involves assuming that the x and t dependence of the disturbance has the normal mode form $\exp[ik(x-ct)]$, in which k is the horizontal wavenumber and c is the phase velocity. The result is an eigenvalue problem for k and c involving an ordinary differential equation with independent variable z, which is called the Taylor–Goldstein equation.

In Holmboe's (1962) analysis, the continuous profiles (1) were approximated by the piecewise linear profiles which are illustrated in Figure 1 by the dashed lines. This simplification permits the z-dependence of the solution to be calculated analytically and, since the x-dependence is removed by Fourier transformation, leaves t as the only independent variable. The necessity of assuming a particular form for the time dependence is thus avoided. In this section we describe the results of normal mode analysis; results from Holmboe's work will be discussed later. In the present study, linear theory is relevant only insofar as it provides guidance in our choice of initial parameter values for the nonlinear simulations, and we shall restrict our discussion of linear theory accordingly; a more detailed explo-

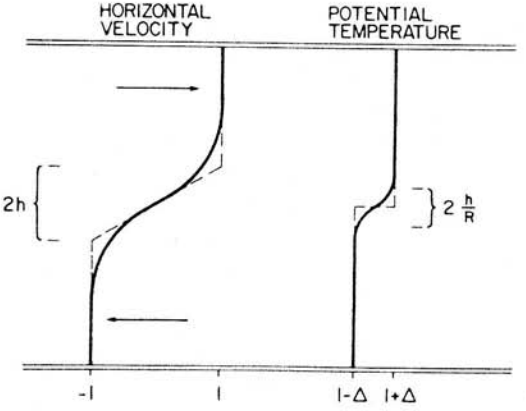

Figure 1 Profiles defining a stably stratified parallel shear flow. Smooth curves are the 'tanh' profiles defined by equation (1); dashed curves are the piecewise-linear approximation used in analytical calculations.

ration of the linear model will be the subject of a subsequent publication.

We begin by nondimensionalizing the problem using u_0 and h as length and velocity scales. Combining the linearized field equations in the usual fashion, we obtain a two-point boundary value problem

$$\hat{w}'' + [(U-c)^{-2}U'^2 Ri - (U-c)^{-1}U'' - \alpha^2]\hat{w} = 0; \quad \hat{w}(\pm\infty) = 0, \quad (3)$$

in which U, c, α, and z are the nondimensional background velocity, phase speed, horizontal wavenumber and vertical coordinate respectively, $\hat{w}$ is the z-dependent complex amplitude of the nondimensional vertical velocity, and the primes denote differentiation with respect to z. The gradient Richardson number Ri is defined by

$$Ri(z) = gh(\ln\theta)'/u_0^2 U'^2, \quad (4)$$

and we define in addition a bulk Richardson number J, which is characteristic of the initial state as a whole, by

$$J = Ri(0) = \Delta R g h/u_0^2. \quad (5)$$

(3) constitutes an eigenvalue problem which implicitly defines a dispersion relation $c = c(\alpha; J, R)$, or equivalently $\sigma = \sigma(\alpha; J, R)$ in which $\sigma = -i\alpha c$ is the exponential growth rate, for a background flow defined by the values of J and R.

We have solved (3) numerically using a parallel shooting algorithm similar to that described by Hazel (1972). The ODE is integrated by means of a sixth-order Runge–Kutta–Fehlberg routine (Enright *et al.*, 1974), and the roots of the secular determinant, which define the eigenvalues, are found using a quadratic interpolation scheme.

The stability characteristics of the flow depend strongly on the value of the scale ratio R. When $R \sim 1$, the flow is stable for J greater than some critical value $J_c(R)$, and it is unstable to Kelvin–Helmholtz waves for $J < J_c$. For $R = 1$, $J_c = 1/4$. When R exceeds a critical value R_c, the flow becomes unstable for all J, with Holmboe instability appearing in the region $J > J_c$. The precise value of R_c is not known, and it is difficult to determine numerically, but application of the Miles–Howard theorem (Miles, 1961; Howard, 1961)

reveals that $R_c > 2$ is a necessary (though not sufficient) condition in order that instability should be possible for all J, as we now show. The gradient Richardson number profile (3) corresponding to the velocity and potential temperature profiles (1) is

$$Ri(z) = J \operatorname{sech}^2 Rz / \operatorname{sech}^4 z. \tag{6}$$

As $|z| \to \infty$, (6) becomes $Ri(z) \simeq \frac{1}{4} J \exp[2(2-R)|z|]$. If $R > 2$, there is always a region in the flow throughout which $Ri < 1/4$, and thus instability is possible for any value of J.

Numerical calculations at various values of R have enabled us to place an upper bound of 2.5 on R_c. Larger values of R than this are needed to obtain Holmboe waves with appreciable growth rates, but setting R too large in a numerical simulation places excessive demands on the resolution, as it leads to the development of inversions which are extremely thin relative to the shear layer depth. These competing considerations have led us to choose the value $R = 3$ for the simulations to be described in what follows.

Figure 2a shows the real and imaginary parts of σ as functions of α and J for $R = 3$. (The stability diagram shown in Figure 2b incorporates the effects of diffusion and horizontal boundaries. It will be discussed in detail later in this section.) Eigenvalues σ occur in complex conjugate pairs, and when σ_i, the imaginary part of σ, is nonzero, the corresponding eigenfunctions describe disturbances which propagate in opposite directions with phase speed equal to $\alpha\sigma_i$. The right-going disturbance has its largest amplitude in the upper region of the shear layer, while the left-going disturbance is strongest in the lower region. Near the centre of the shear layer, the amplitudes of the two disturbances are similar, and they thus interfere to create the effect of a standing wave, with oscillation frequency equal to σ_i. Oscillatory (Holmboe) instabilities are thus predicted in the upper part of the unstable region shown in Figure 2a, where σ is complex. For smaller J, σ is real, and we thus expect a stationary (Kelvin–Helmholtz) instability. The numbered points indicate parameter values for which nonlinear simulations have been performed. We predict on the basis of Figure 2a the appearance of a rapidly oscillating Holmboe wave at point 1, a more slowly oscillating Holmboe wave at point 2, and a Kelvin–Helmholtz wave at point 3.

We turn now to an examination of the effects of diffusion on the background flow. The background profiles (1) are not a steady state

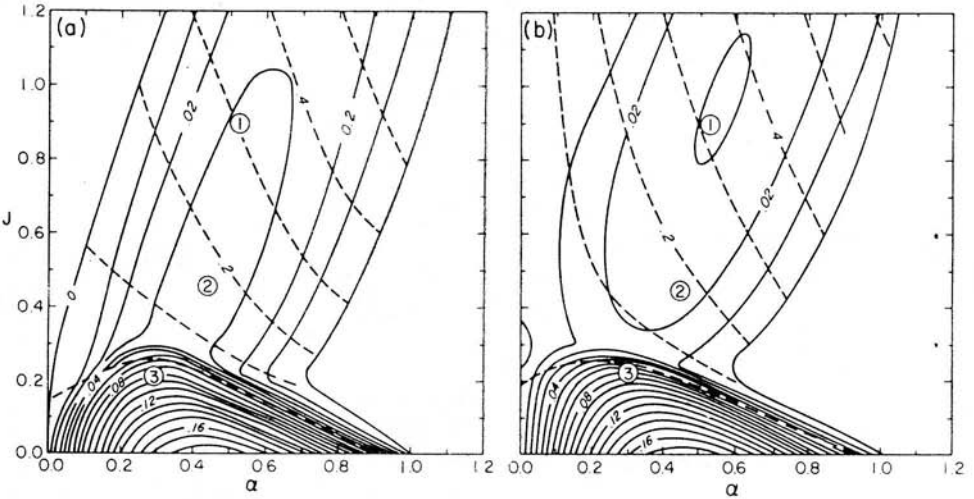

Figure 2 Dispersion relation $\sigma(\alpha, J)$ for tanh profiles with $R=3$. Smooth curves are contours of the growth rate σ_r; dashed curves are contours of the oscillation frequency σ_i. (a) is the inviscid, vertically unbounded case; (b) is the diffusive, vertically bounded case with $Re=300$, $Pr=9$ and frictionless insulating boundaries placed at a distance $5h$ above and below the centre of the shear layer.

solution of the hydrodynamic equations if the effects of nonzero viscosity and thermal conductivity are included. Diffusive effects cause the tanh profiles to broaden in time and thus modify the stability characteristics of the flow. The implications of this time-dependence must be taken into account when we choose initial parameter values for the nonlinear simulations.

The evolution of a purely horizontal velocity profile $U(z,t)$ under the influence of diffusion is governed by the usual linear equation

$$\partial U/\partial t = Re^{-1}\partial^2 U/\partial z^2, \tag{7}$$

in which Re is the Reynolds number hu_0/ν and ν is the kinematic viscosity. A simple solution to (7) which closely approximates our tanh velocity profile is

$$\tilde{U}(z,t) = \operatorname{erf}[\tfrac{1}{2}\pi^{1/2} z/h(t)]; \quad h(t) = (1 + Re^{-1}\pi t)^{1/2}. \tag{8}$$

The half-depth h/R of the stratified layer evolves in a similar fashion,

$$h(t)/R(t) = R_0^{-1}[1 + R_0^2(RePr)^{-1}\pi t]^{1/2}, \tag{9}$$

where Pr is the Prandtl number ν/κ, κ is the thermal diffusivity, and $R_0 = R(0)$. Combining these results, we find

$$R(t) = R_0\{(1 + Re^{-1}\pi t)/[1 + R_0^2(RePr)^{-1}\pi t]\}^{1/2}. \tag{10}$$

Note that the Reynolds number which appears in Eqs. (7) through (10) is computed using the initial half-depth of the shear layer in dimensional units. As the initial profiles diffuse, the flow becomes more nearly inviscid as the "effective" Reynolds number increases in proportion to $h(t)$.

In the present context, the most important effect of mean flow diffusion is the evolution of the scale ratio $R(t)$, as described by Eq. (10). We must choose values of Re and Pr for the nonlinear simulations in such a way as to ensure that R remains significantly larger than the critical value, $R_c \sim 2.5$, for a sufficient length of time so that the Holmboe wave may grow to finite amplitude. It is clear from Eq (10) that if R is equal to $Pr^{1/2}$ at $t=0$, it remains equal to $Pr^{1/2}$ for all time. If R has some other value initially, it approaches the value $Pr^{1/2}$ asymptotically on a time scale proportional to Re. In the atmosphere, $Pr \sim 1$, so that a stratified shear flow must eventually become stable to Holmboe waves, but as Re is typically very large in such flows, Holmboe waves have ample time to grow. However, such extreme Reynolds numbers cannot be managed by a numerical model with the computer memory currently available. Instead, we suppress the time dependence of R entirely by setting $Pr = 9$ (with $R_0 = 3$, as discussed earlier). With this value of Pr, an initial Reynolds number of 300 is easily manageable by our numerical model, and is large enough to permit the evolution of the waves in which we are interested. It will be noted that with $Re = 300$ and $Pr = 9$, we are actually modelling something very similar to a laboratory-scale flow. (The salt-stratified water used in laboratory experiments has $Pr \sim 700$, but $Pr = 9$ should be sufficiently large to yield similar behavior.) We assume that geophysical flows evolve in essentially the same manner.

In Figure 2b, we display the results of a normal-mode stability analysis incorporating the effects of viscosity and heat conduction. The calculation was performed using a two-dimensional version of

the algorithm described in Klaassen and Peltier (1985b). The parameter values $Re=300$ and $Pr=9$ were chosen in accordance with the considerations discussed above.

In addition, we have included frictionless insulating boundaries located at a distance $5h$ above and below the centre of the shear layer. Figure 2b shows that the presence of boundaries destabilizes the flow at low values of α, in accordance with the inviscid results of Hazel (1972), but it has little effect on the wavenumber and the growth rate of the fastest-growing mode at each J.

It is evident upon comparison of Figures 2a and 2b that the level of diffusion considered here does not alter the qualitative stability characteristics of the flow. The regimes of Kelvin–Helmholtz and Holmboe instability still exist and are located in regions of the $J-\alpha$ plane close to those found in the inviscid case. In addition, there is no significant change in the wavenumber of the fastest-growing mode at any J. However, diffusion alters the numerical values of the growth rates to a substantial degree. For very strong stratification (J greater than about 0.9 in this case), diffusion tends to increase σ_r, while σ_r decreases in the presence of diffusion at lower values of J. One important result of this is that the local maximum of the growth rate in the Holmboe wave regime is shifted from $J\sim0.45$ to $J\sim0.95$, and becomes much more sharply defined. We will turn next to a discussion of the dimensionality of the primary Holmboe instability, and we will see that this sharpening of the local maximum of the growth rate may have important implications in this context.

To this point, we have assumed implicitly that the fastest-growing mode of instability is two-dimensional (i.e. there is no dependence on the spanwise coordinate y), as is traditional in consequence of Squire's theorem (Squire, 1933; Yih, 1955). In this case, however, we are concerned with an instability whose growth rate increases with increasing stratification in some regions of the $J-\alpha$ plane, as is evident on inspection of Figure 2b. This fact requires that we examine the assumption of two-dimensionality in some detail.

A plane wave propagating at an angle ϕ from the x-direction is only affected by the component of the background shear which is parallel to its wave vector, i.e. it "sees" a background velocity profile $U(z)\cos\phi$. The behavior of such a wave is easily deduced from that of a two-dimensional wave with the same wavelength by employing

"effective" values of the relevant nondimensional parameters, which are computed using the reduced velocity scale $u_0 \cos\phi$. The results are summarized in the following relation:

$$\sigma(\alpha, \phi, J_1, R) = \cos\phi \cdot \sigma(\alpha, 0, J_2, R), \tag{11}$$

in which $J_2 = J_1/\cos^2\phi$ and $\sigma = \sigma(\alpha, 0, J, R)$ is the two-dimensional dispersion relation calculated earlier. In a viscous normal-mode analysis, the effective Reynolds number is $Re\cos\phi$. By setting $J=0$ in (11) (which makes R irrelevant), we recover Squire's theorem.

The Holmoe instability, being dependent on stratification for its existence, has zero growth rate when $J=0$. *As* J increases, σ_r increases to a maximum, then decreases asymptotically to zero at very large J. As has been pointed out by Browand and Wang (1972) and more recently by Lawrence *et al.* (1987), this increase in growth rate with increasing J introduces the possibility that the fastest-growing mode at a given (α, J) may have $\phi \neq 0$. These instabilities occur in pairs with equal growth rates and opposite values of ϕ (i.e. $\phi_2 = -\phi_1$), which interfere to generate waveforms which are periodic in the spanwise direction. The waves observed in the laboratory experiments of Lawrence *et al.* (1987) strongly suggest the presence of this three-dimensional primary instability. We must point out, however, that positive $\Delta\sigma_r/\Delta J$ does not automatically imply three-dimensionality, owing to the factor $\cos\phi$ which multiplies the right-hand side of (11). We expect a three-dimensional instability to be observed on a flow with $J = J_1$ if and only if

$$d(\sigma_r/J^{1/2})/ds\big|_{J=J_1} > 0. \tag{12}$$

Here, σ_r is evaluated on the curve defined by the locus of all points at which σ_r is maximized with respect to α, and the derivative d/ds is taken along this curve in the direction of increasing J.

For the piecewise-linear model considered by Holmboe (1962) and by Lawrence *et al.* (1987; cf. Figure 1 of this paper), we show in the Appendix that the inequality (12) is not satisfied at any point in the Holmboe wave regime. For the more realistic model considered here (i.e. smooth profiles of velocity and potential temperature in a viscous, heat conducting, vertically bounded flow), the corresponding calculation must be done numerically and will be deferred to a later

publication. For "tanh" profiles in an inviscid flow, the stability characteristics of which are illustrated in Figure 2a, the local maximum in σ_r is clearly too weak for (12) to be satisfied at any J_1. However, the sharpening of the local maximum in σ_r due to diffusion, which was noted in the discussion of Figure 2b, leads us to suspect that the fastest-growing Holmboe instability may in fact be three-dimensional when the Reynolds number is sufficiently small.

An alternative explanation for the three-dimensionality observed in the laboratory experiments of Lawrence *et al.* (1987) is that the Holmboe wave is modified at an early stage of its evolution by the emergence of a three-dimensional secondary instability. We plan to investigate both of these alternatives in detail in the near future, but for purposes of the present paper we shall restrict our attention to the evolution of two-dimensional instabilities.

3. METHODOLOGY

The numerical model which we employ is based on the anelastic approximation to the hydrodynamic equations. The thermodynamic fields T, θ, ρ, and p are expanded about a hydrostatic reference state in which the potential temperature is equal to a constant, Θ. We nondimensionalize using temperature scale Θ, density scale ρ_0, pressure scale $\rho_0 u_0^2$, with velocity and length scales u_0 and h as before. The expansions for the field variables are then

$$T(x,z,t) = \bar{T}(z) + T'(x,z,t), \tag{13a}$$

$$\theta(x,z,t) = 1 + \Delta\theta^*(x,z,t), \tag{13b}$$

$$\rho(x,z,t) = \bar{\rho}(z) + \rho'(x,z,t), \tag{13c}$$

$$p(x,z,t) = \bar{p}(z) + p'(x,z,t), \tag{13d}$$

with

$$d\bar{p}/dz = -\bar{\rho}g, \quad \bar{T}(\bar{p}/p_0)^{-R_d/C_p} = 1, \quad \bar{p} = \bar{\rho}R_d\bar{T}, \tag{14}$$

in which R_d and C_p are the gas constant and specific heat capacity at constant pressure for dry air. Note that the nondimensional potential

temperature deviation θ^* is expressed as a fraction of its maximum value Δ. At $z=0$, we have $p=p_0$ and $\bar{T}=1$. Although it is assumed in this formulation that the fluid is an ideal gas, the results apply equally well to liquids provided that departures from the reference state are small. Solutions to (14) for the thermodynamic reference fields are easily derived, and are nearly constant for our application, since the domain height employed is only a small fraction of the isentropic scale height C_p/g. It may be shown (Batchelor, 1953; Ogura and Phillips, 1962) that the velocity field $u_i(x,z,t)$, $i=1,3$ and the deviations of the thermodynamic fields from the reference state (provided that the latter are small) obey the following set of equations:

$$Du_i/Dt = -\bar{\rho}\partial p'/\partial x_i - C^{-2}gp'\delta_{i3} + R^{-1}J\theta^*\delta_{i3} + (Re)^{-1}\partial(D_{ij})/\partial x_j, \tag{15a}$$

$$\partial(\bar{\rho}u_j)/\partial x_j = 0, \tag{15b}$$

$$D\theta^*/Dt = (RePr)^{-1}\partial^2\theta^*/\partial x_j^2, \tag{15c}$$

in which

$$D_{ij} \equiv \partial u_i/\partial x_j + \partial u_j/\partial x_i - (2/3)\delta_{ij}\partial u_k/\partial x_k. \tag{16}$$

Equations (15) form a closed set of four nonlinear PDE's for the unknown fields u_1, u_3, p', and θ^*, which depend on the variables x, z, and t. Boundary and initial conditions in the three independent variables are as follows:

(1) In the x-direction, we impose periodicity $f(x+\lambda,z,t)=f(x,z,t)$ for each field, with the nondimensional wavelength $\lambda=2\pi/\alpha$ equal to that of the fastest-growing mode of linear theory, as described in Section 2.

(2) At $z=0$ and $z=H$, we place horizontal, frictionless, insulating boundaries on which the following conditions obtain:

$$\partial(\bar{\rho}u_1)/\partial z = u_3 = 0, \qquad D_{ij} = 0, \tag{17a}$$

$$\partial\theta^*/\partial x = \partial(\bar{\rho}\partial\theta^*/\partial z)/\partial z = 0, \tag{17b}$$

$$\partial p'/\partial z = -(C^2\bar{\rho})^{-1}gp' + R^{-1}J\theta^* + (\bar{\rho}Re)^{-1}\partial(\bar{\rho}D_{zz})/\partial z. \quad (17c)$$

(3) At $t=0$, the dependent fields are assumed to consist of two components, namely the hyperbolic tangent background profiles and a fluctuation from which the instability is initiated. The background profiles are:

$$u_1 = \tanh(z-\tfrac{1}{2}H), \quad u_3 = 0, \quad \theta^* = \tanh R(z-\tfrac{1}{2}H), \quad (18)$$

in which the scale ratio R is set equal to 3.0 and the value of J is chosen according to the results of linear stability analysis, as shown in Figure 2. In order to conserve computational resources, we provide the instability with a head start by initializing the fluctuation not as random noise but rather as a weak perturbation whose structure is determined by the eigenfunctions of the fastest-growing mode of linear stability theory. In the case of Holmboe instability, the initial perturbation is a superposition of two distinct eigenmodes which have equal growth rates and equal but opposite horizontal phase velocities, as was discussed in Section 2. The initial amplitudes of the nodes are set equal, while the initial phase relationship between them is chosen arbitrarily.*

This completes the description of the mathematical model employed for the nonlinear simulations to be reported here. The numerical algorithms employed to solve the model equations are described in general in Clark (1977), and specifically for application to the stratified parallel flow problem in Peltier *et al.* (1978). The model has been previously employed to simulate nonlinear mountain waves (e.g. Peltier and Clark, 1979) as well as for the Kelvin–Helmholtz wave studies (e.g. Davis and Peltier, 1979; Klaassen and

*It might be supposed that the phase relationship between the two eigenmodes at $t=0$ could play an important role in determining the future evolution of the wave. We do not believe that this is so, for the following reasons. In most of the Holmboe wave regime, and in particular at points 1 and 2 of Figure 2, the rate at which the right-going and left-going modes pass by one another is considerably greater than the growth rate (i.e. $|\sigma_i| \gg \sigma_r$), hence the wave undergoes many oscillations in the process of growing to large amplitude and the point in the cycle at which the simulation is begun is not likely to be important. This argument becomes invalid as one approaches the KH-Holmboe transition (between points 2 and 3 of Figure 2) and $|\sigma_i|$ drops to zero, but in this limit the two eigenmodes become indistinguishable in vertical structure, so that the initial phase relationship between them is once again of little importance.

Peltier, 1985a) of which the present work is an extension. The fields are evaluated on either a 128×128 or a 256×256 staggered grid, and stepped forward in time using a leapfrog scheme with time step chosen small enough to satisfy the Freidrichs–Loewy–Courant condition. At appropriate intervals in each simulation the velocity, pressure, and temperature fields are saved for later analysis.

Diagnostics to be employed in our analyses fall into three groups: full space and time dependent fields, horizontal averages of these fields which depend on the vertical coordinate and time, and integrated quantities which depend on time only. The fields selected to represent the flow for present purposes are the potential temperature deviation $\theta^*(x,z,t)$ and the vorticity $\zeta(x,z,t) = \partial u_3/\partial x - \partial u_1/\partial z$. Potential temperature will be visualized by means of contour plots. Since thermal diffusion is relatively weak in these flows, the contours behave very much like dye lines in a laboratory flow. The vorticity field is represented by continuous shading, using a high resolution palette from white to black. This emphasizes the locations and magnitudes of the local extrema, which are features of primary interest, much more clearly than contour plots. These two plots are superimposed, providing an economical and detailed representation of the appearance and underlying dynamics of the flow.

A feature of the potential temperature field which is of particular interest in the study of Holmboe waves is the motion of the points at which θ^* is an extremum with respect to x for a given value of z. With the proper choice of z, these x-values indicate the positions of the oppositely propagating component disturbances which constitute the Holmboe wave. The position of the minimum in θ^* at a height slightly above the centre of the domain, and that of the maximum at a height slightly below the centre, are tracked continuously during the simulations.

We monitor the evolution of four horizontally averaged quantities—the velocity (which has a nonvanishing average in the x-direction only) $\bar{U}(z,t)$, the potential temperature $\overline{\theta^*}(z,t)$, the Reynolds stress $\bar{\rho}\overline{u_1' u_3'}$ and the vertical heat flux $R^{-1}J\bar{\rho}\overline{\theta^* u_3'}$, in which the overbars denote horizontal averages (with the exception of the adiabatic reference density $\bar{\rho}$), and primes indicate deviations from the horizontal average, e.g. $u_1' \equiv u_1 - \bar{U}$. The first two profiles allow us to see how the mean flow evolves in response to the combined effect of diffusion and wave growth. The vertical derivatives of the

latter two quantities measure the contribution of the wave–mean flow interaction to the time tendencies of the horizontally averaged velocity $\bar{U}(z,t)$ and the horizontally averaged potential temperature $\bar{\theta}^*(z,t)$ respectively.

In addition, we shall follow the evolution of a set of integrated quantities associated with the transfer of energy between the mean flow and the wave. We define the mean flow kinetic energy, the wave kinetic energy and the potential energy respectively as

$$\bar{K}(t)=\langle \tfrac{1}{2}\bar{\rho}\bar{u}^2\rangle, \quad K'(t)=\langle \tfrac{1}{2}\bar{\rho}\overline{u_i'u_i'}\rangle,$$
$$P(t)=-R^{-1}J\langle \bar{\rho}z\overline{\theta^*}\rangle, \tag{19}$$

where $\langle * \rangle = \int_0^H * \, dz$.

These quantities may be shown (Klaassen and Peltier, 1985a) to obey an energy closure of the form

$$d\bar{K}/dt = -C(\bar{K},K') - Re^{-1}D(\bar{K}), \tag{20a}$$

$$dK'/dt = C(\bar{K},K') + C(P,K') - Re^{-1}D(K'), \tag{20b}$$

$$dP/dt = -C(P,K') + (RePr)^{-1}D(P). \tag{20c}$$

The quantities $C(\alpha,\beta)$ represent the transfer of energy from reservoir α to reservoir β, and are defined as

$$C(\bar{K},K') = -\langle \bar{\rho}(\partial\bar{u}/\partial z)\overline{u_1'u_3'}\rangle,$$
$$C(P,K') = R^{-1}J\langle \bar{\rho}\overline{\theta^{*\prime}u_3'}\rangle, \tag{21}$$

with $C(\alpha,\beta) = -C(\beta,\alpha)$. Note that $-C(\bar{K},K')$ is the integral over z of the product of the Reynolds stress and the mean shear, while $C(P,K')$ is the integral over z of the vertical heat flux. $D(\alpha)$ represents diffusion of energy from reservoir α, viz:

$$D(\bar{K}) = \langle \bar{\rho}(\partial\bar{u}/\partial z)^2\rangle, \quad D(K') = \langle \bar{\rho}\overline{D_{ij}'D_{ij}'}\rangle,$$
$$D(P) = R^{-1}J\langle \bar{\rho}\partial\overline{\theta^*}/\partial z\rangle. \tag{22}$$

Note that the potential energy of the flow is increased by diffusion, hence the positive sign on the diffusion term in Eq. (13c).

4. RESULTS

We begin the results section by showing a brief selection of diagnostics from each of the three simulations (flows with strong, moderate, and weak stratification, as illustrated in Figure 2), for purposes of comparison. We then present for each simulation a full set of diagnostics chosen to illustrate specific points of interest.

4.1 Overview

The wave kinetic energy histories for the three simulations are shown in Figure 3. It will be noticed first from these data that simulation 3 was terminated at a relatively early stage in the life

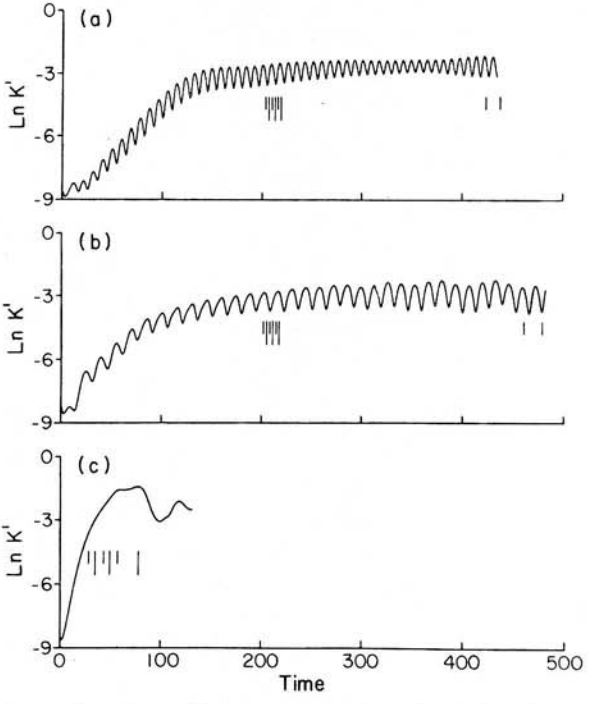

Figure 3 Natural log of wave kinetic energy for (a) point 1, (b) point 2 and (c) point 3. Thin vertical lines mark times for which further data are being presented.

cycle of the wave. This was due to resolution problems which developed in consequence of extreme gradients of velocity and potential temperature, the latter being particularly severe because of the large Prandtl number employed. Similar problems were encountered by Klaassen and Peltier (1985c) in Kelvin–Helmholtz wave simulations with $Re = 500$, $Pr = 1$, $J = 0.07$, and $R = 1$. The wave was well resolved up to maximum amplitude, however, and it is probable that a three-dimensional secondary instability would have developed near this stage (Klaassen and Peltier, 1985b). The first two simulations were well resolved throughout their duration and were stopped only as it became evident that the waves had entered a quasi-equilibrium state dominated by very slow diffusive decay. We will refer later to the thin vertical lines below the $\ln K'(t)$ curves in Figure 3; they indicate specific instants at which further diagnostics will be presented.

Simulations 1 and 2 have clearly generated oscillatory waves, with simulation 1 exhibiting the higher frequency oscillation. Simulation 3 delivered a monotonically growing wave which achieved maximum amplitude much more quickly than did the oscillatory waves. These qualitative features are in agreement with the predictions of linear stability analysis; quantitative comparisons are not as easily interpretable. The oscillation frequencies at points 1 and 2 are both within $\sim 10\%$ of the theoretically predicted values, and remain remarkably consistent throughout the duration of the simulations. Exponential growth rates may be measured approximately by fitting a straight line to $\ln K'(t)$ in the region where it is most nearly linear (apart from the periodic oscillations). For simulations 1 and 2, this is between $t \sim 50$ and $t \sim 100$. The growth rate is then given by $\sigma_r = \frac{1}{2} d[\ln K'(t)]/dt$. In simulation 1, the growth rate is about 30% lower than expected. The growth rate in simulation 2 agrees with theory to within a few percent, and the stationary wave at point 3 grows about 20% faster than linear theory predicts. The growth rates and frequencies observed in the simulations thus agree with the predictions to the extent one would expect in light of the considerations discussed at the end of Section 2.

Finally, it will be observed that the kinetic energy which the wave achieves in these experiments is largely independent of the level of stratification present. Although the Holmboe waves have much smaller linear growth rates than do KH waves, they are apparently

able to grow exponentially for a correspondingly longer time before nonlinear damping sets in, and they thus achieve a much larger amplitude than might be expected on the basis of their small linear growth rates. A similar phenomenon has been observed in simulations of asymmetric flows, where one component of the Holmboe instability has a larger growth rate than the other, yet achieves a comparable amplitude.

In Figure 4, we present contour plots of the potential temperature field at three different times for each of the three simulations. The times are indicated in Figure 3 by the longer vertical lines below the $\ln K'(t)$ curves. The upper contour line corresponds to $\theta^* = 0.9$, i.e. 90% of the maximum deviation of the potential temperature field from its mean value. The lowest contour represents $\theta^* = -0.9$, and the other contour values are spaced equally between these extremes. The central temperature interface is darkened for emphasis. These conventions will be followed in all the contour plots of potential temperatures that we present. Figures 4a and 4b show the oscillatory waves at points 1 and 2, respectively, of Figure 2, as they evolve through approximately one half-cycle near the time when maximum wave kinetic energy is achieved. In Figure 4c, we see the stationary disturbance at point 3 performing the characteristic roll-up of the Kelvin–Helmholtz wave.

The Holmboe wave at point 1 has a relatively simple structure. The oppositely propagating component waves predicted by linear theory are clearly visible, as is the standing oscillation of the central temperature interface. Note the highly localized form of the component waves. Using the terminology of solitary waves, we will refer in what follows to the outer extremities of the component waves as "crests", even though the "crest" of the lower wave extends downward. At point 2, we observe the ejection of thin plumes of stratified fluid into the regions above and below the shear layer, a phenomenon which is commonly observed in laboratory experiments (e.g. Browand and Wang, 1972; Lawrence *et al.*, 1987). As we will see below, there is a concentration of clockwise vorticity in the lee of each component wave, and the plumes are formed when these vortices are strong enough to entrain stratified fluid from the downstream faces of the component waves. At point 1, the strength of the stratification relative to the shear (i.e. the bulk Richardson number) is relatively large, and the vortices are thus unable to

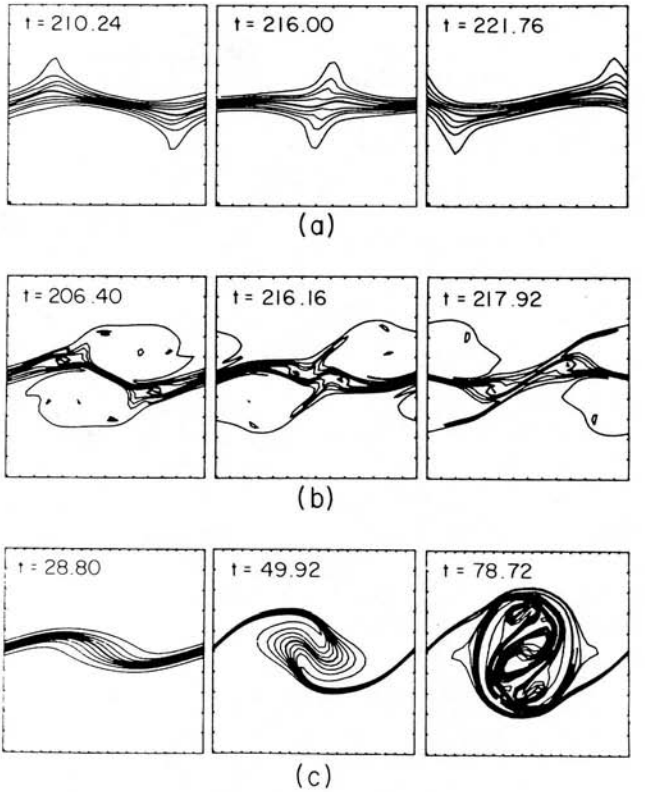

Figure 4 Contours of potential temperature deviation at sample times for simulations 1, 2, and 3. Top contour is $\theta^* = 0.9$; bottom contour is $\theta^* = -0.9$.

entrain enough fluid to form a visible plume. The plumes shown in Figure 4b are not permanent features; they subside as the component waves pass each other and are regenerated in the next half-cycle as the waves approach each other once again. The reasons for this behavior will be discussed later when we examine the results of simulation 2 in detail.

It is clear from Figure 2 that as we decrease the level of stratification in this sequence of experiments, the phase speeds of the upper and lower component waves should decrease, going ultimately to zero at point 3. In the latter case, the component waves become phase-locked, and wrap around each other to form the usual

Kelvin–Helmholtz vortex. Holmboe (1962) examined this mechanism in more detail, showing that the phase speeds of the component disturbances in a Holmboe wave are not constant, but rather oscillate along with the oscillation of the waveform. The weaker the stratification, the more pronounced the variations in phase speed become. This is readily understood if one thinks of the thin stratified layer as a boundary between the component waves. When the stratification is strong, the waves propagate independently of one another and thus the phase speed is the same at all points in the cycle. With weaker stratification, the waves interact and the phase speeds thus vary with the configuration.

This prediction may be verified by inspection of Figure 5, in which the trajectories of the component waves in the early linear regime are plotted for simulations 1 and 2. Note that the length and time scales of the graphs have been adjusted so that the average slopes of

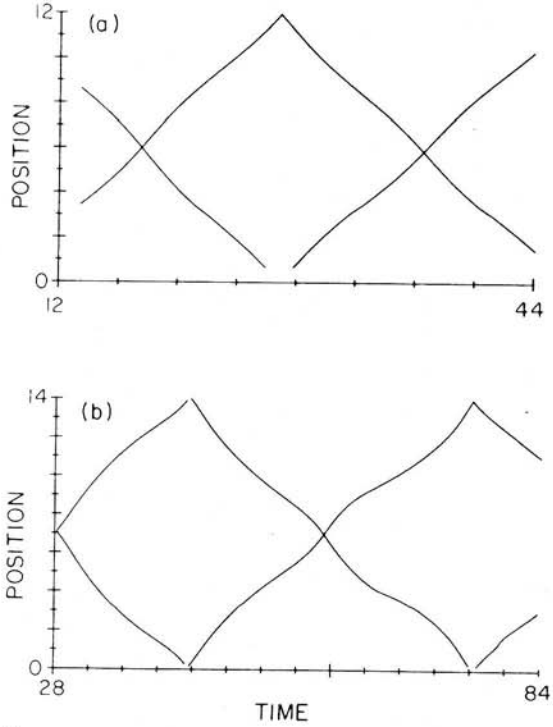

Figure 5 Component wave trajectories for (a) simulation 1 and (b) simulation 2.

the trajectories in the two cases appear equal, in order that we may compare visually the relative variability of the phase speeds. The variations in phase speed are clearly much greater in the moderately stratified flow than in the strongly stratified flow, as predicted. We note further that the component waves move fastest as they are passing each other, and slowest when they are widely separated. As we reduce the stratification, it is in this latter configuration that the instantaneous phase speeds first vanish, and that the component disturbances will become phase-locked to form the Kelvin–Helmholtz wave. (If we initialized a Kelvin–Helmholtz wave simulation with two component waves in some other configuration, one above the other, for example, the waves would propagate horizontally until the appropriate configuration was reached before becoming phase-locked.) The validity of these predictions may be verified by examining the first frame of Figure 4c, where we see two component waves, well separated from each other (compare with frame 1 of Figure 4a), and just beginning to roll up.

4.2 The time-dependent structure of a Holmboe wave in a strongly stratified flow

We turn now to a detailed examination of the Holmboe wave at point 1 of Figure 2. In the analysis of this simulation, we are able to focus on the essential dynamics of the Holmboe wave in the absence of plume ejection. The complete instantaneous energy budget for the point 1 wave is plotted in Figure 6. The top frame shows the energy reservoirs $\bar{K}$, K', and P as well as the total energy $T=\bar{K}+K'+P$. Note that the values of $\bar{K}$, K', and T have been adjusted for ease of presentation. The two vertical lines which intersect the three frames of Figure 6 indicate sample points in the wave's evolution at which the waveform exhibits the extreme configurations: the left-hand line corresponds to a point at which the upper and lower component waves are just passing each other, while the right-hand line shows the subsequent time at which the waves are maximally separated. The potential temperature field at approximately these times is shown in frames 2 and 3 of Figure 4.

As is evident from Figure 6, the total energy of the wave at point 1 decreases monotonically due to diffusion. The oscillatory behavior of the wave corresponds to a periodic exchange of energy between

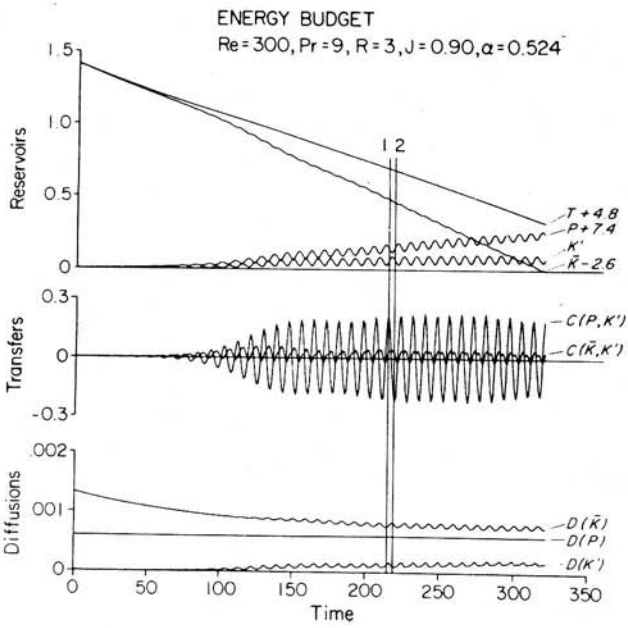

Figure 6 Energy budget for simulation 1. Vertical lines mark sample times at which waves are (1) minimally separated, (2) maximally separated.

the three reservoirs, primarily between the wave kinetic energy and the potential energy. The weak oscillations in $\bar{K}$ are due to the fact that the wave extracts energy from the mean flow most efficiently just after the component waves have passed each other. In the middle frame of Figure 6, we see again that the dominant energy exchanges are between K' and P, but note that the transfer from $\bar{K}$ to K' is nearly positive definite, and its cumulative effect is responsible for the growth of the wave. Once the wave has reached large amplitude, the part of the cycle during which $C(\bar{K}, K')$ is large divides into two intervals of similar duration. During the first interval, the component waves have just passed each other, and the wave is gaining kinetic energy both from the mean flow and from the potential energy reservoir. In the second interval, the component waves are approaching each other once again, and the kinetic energy which the wave extracts from the mean flow, along with some of the kinetic energy it has accumulated previously, is being converted into potential energy.

The diffusion terms are shown in the bottom frame. Recall that $D(P)$ represents an increase in potential energy, since diffusion in a stably stratified environment works, on the average, to move mass upward. It is clear that diffusion plays only a minor role in the evolution of the flow as a whole once the wave has reached finite amplitude, but it works constantly to dissipate energy at the smaller scales of the motion and thus to cause the eventual decay of the wave.

In Figure 7, we show the potential temperature and vorticity fields for the wave at point 1 evolving through one half-cycle of a typical oscillation. Again, the potential temperature contours are spaced equally between $\theta^* = 0.9$ and $\theta^* = -0.9$. The dark-shaded regions correspond to counter-clockwise rotation, while light shading denotes clockwise rotation. The intermediate shade of grey found near the upper and lower edges of the domain represents irrotational motion.

Underresolution is primarily responsible for the alternating dark and light fringes which are visible in the vorticity field behind each component wave crest. This simulation was run on a 128×128 grid,

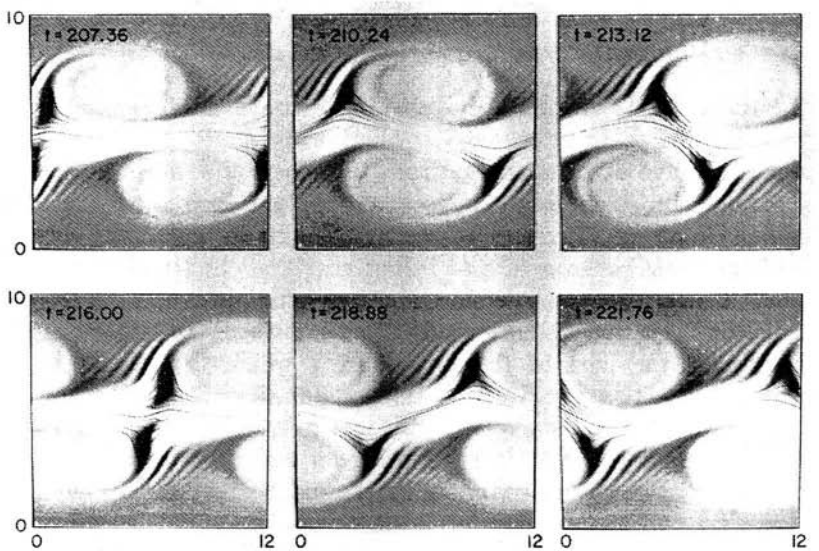

Figure 7 Potential temperature and vorticity fields for simulation 1. White (black) indicates clockwise (counter-clockwise) rotation. Potential temperature contours are as in Figure 4.

while 256×256 grids were used for the simulations at points 2 and 3. The Holmboe wave at point 2 is very well resolved and shows no fringes, while Holmboe waves simulated on grids of 128×128 points or less develop fringes consistently. The fringes do not appear to influence the evolution of the wave in any important way.

The concentrations of clockwise vorticity in the lee of each component wave, which we referred to in the discussion of plume ejection in Secton 4.1, are clearly visible. Stronger concentrations of clockwise vorticity occur in the vicinity of the central temperature interface, while counter-clockwise rotation is found primarily in the crests of the component waves.

In Figure 8, the profiles of horizontally averaged potential temperature deviation, velocity, Reynolds stress, and vertical heat flux are shown for the times indicated in Figure 7. The potential temperature and velocity profiles vary little during the cycle but the latter two profiles, as they involve deviations from the mean fields, show a clear periodic variation. The largest Reynolds stresses occur as the component waves pass each other (frames 1 and 4 of Figures 7 and 8), at which time there is a vertical flux of horizontal momentum out of the upper and lower regions of the shear layer, where the Reynolds stress is negative, and into the centre of the shear layer, where the Reynolds stress is positive. As the waves move apart, these fluxes are reversed. At this time there is also a strong flux of heat out of the central region of the shear layer, which is subsequently reversed as the component waves approach each other once again. Note that the rate $C(\bar{K}, K')$ at which kinetic energy is extracted from the mean flow is the product of the negative of the Reynolds stress and the mean shear, integrated in the vertical. Since the mean shear is largest at the centre of the domain, $C(\bar{K}, K')$ is largest when the Reynolds stress is large and negative at that point. This occurs in frames 2 and 5, which correspond of the state of maximum separation of the component waves. As we saw in Figure 6, this is indeed the point in the cycle where the wave extracts kinetic energy most efficiently from the mean flow. It is evident from the Reynolds stress profiles that the configuration in which the waves are just passing each other (frames 1 and 4) is well suited for the extraction of energy from the mean flow near the edges of the shear layer. The shear in those regions is weak, however, and $C(\bar{K}, K')$ is correspondingly small at that point in the cycle.

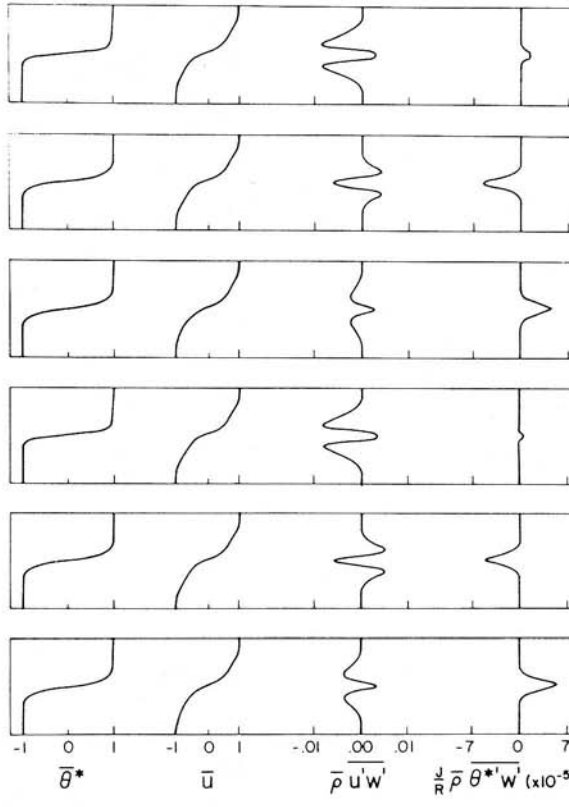

Figure 8 Horizontally averaged profiles of potential temperature deviation, velocity, Reynolds stress, and vertical heat flux corresponding to the times shown in Figure 7.

We conclude the description of simulation 1 with a brief look at the wave in the later stages of its evolution. In Figure 9 we show the potential temperature and vorticity fields and the four horizontally averaged profiles at two points late in the simulation, as indicated by the final two pointers in Figure 3a. We notice first that the vertical symmetry about the centre of the domain which was apparent at earlier times has been broken. This did not occur in either of the other two simulations, and it is probably due to the inertial effects of the strong stratification, i.e. to the fact that a symmetrically distributed force causes a slightly larger acceleration in the lighter fluid near the top of the domain than in the dense fluid near the bottom. Once the symmetry has been broken, one component of the

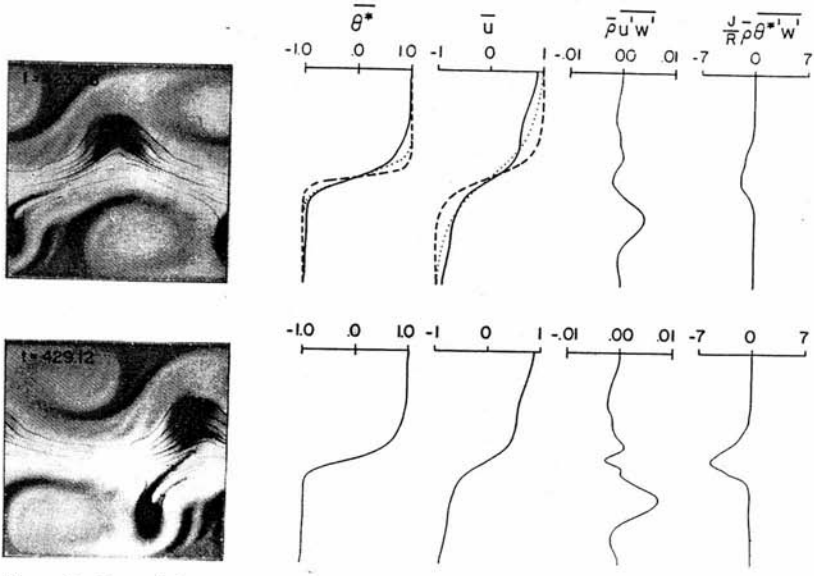

Figure 9 Potential temperature, vorticity, and horizontally averaged profiles in the later stages of simulation 1. Dashed curves indicate profiles at $t=0$; dotted curves show profiles which would obtain at the current time in the absence of wave growth, as determined by Eqs. (23) through (25).

Holmboe wave gradually disappears, while the other component evolves into a sharp-crested interfacial wave of the type described by Thorpe (1968b). This process will be described in detail in a separate publication devoted to the evolution of shear instabilities on asymmetric flows. The effects of diffusion and wave growth on the horizontally averaged profiles of potential temperature and horizontal velocity may be compared by inspection of the dashed and dotted curves in Figure 9. The dashed curves indicate the profiles at $t=0$, while the dotted curves represent the profiles which would obtain at $t=423.36$ in the absence of wave growth, i.e. if the evolution of the flow was due only to diffusion. The dotted curves were computed numerically from the diffusion equations

$$\partial\bar{U}/\partial t = Re^{-1}\partial^2\bar{U}/\partial z^2, \quad \partial\bar{\theta}^*/\partial t = (RePr)^{-1}\partial^2\bar{\theta}^*/\partial z^2, \tag{23}$$

with boundary conditions

$$\partial\bar{U}/\partial z = \partial\bar{\theta}^*/\partial z = 0 \quad \text{at } z=0, H \tag{24}$$

and initial conditions

$$\bar{U}(z,0)=\tanh z, \quad \bar{\theta}^*(z,0)=\tanh Rz. \tag{25}$$

It is evident upon inspection of the $\bar{\theta}^*$ profiles that thermal mixing due to wave growth occurs primarily in the crest of the upper component wave. Thermal mixing near the centre of the shear layer is due almost entirely to diffusion. Near the outer edges of the domain, the $\bar{\theta}^*$ profile has evolved very little since $t=0$. In contrast, the $\bar{U}$ profiles reveal that momentum mixing has occurred throughout the domain, due primarily to diffusion near the centre of the domain, and to wave action near the boundaries.

4.3 The time-dependent structure of the Holmboe wave in a moderately stratified flow

As we saw in Figure 4, the behavior of the Holmboe wave at point 2 of Figure 2 is strikingly different from that of its counterpart at point 1, yet upon examination of the energy budget for the former (Figure 10, compare with Figure 6), one notices little difference from the more strongly stratified case. The differences which are visible in the potential temperature fields consist primarily of small scale flow structures which develop in consequence of the reduced level of stratification, and whose effects are not readily apparent in the spatially averaged quantities which make up the energy budget.

The reduction in oscillation frequency is readily apparent, and is reflected in the fact that the rate of energy transfer between the wave kinetic and potential energy reservoirs, $C(P,K')$, is relatively small, although inspection of the P and K' curves reveals that the amount of energy exchanged in each oscillation is nearly the same as it was in simulation 1. The points in time at which plume ejection occurs coincide with the points at which $C(P,K')$ is large and negative. The latter condition indicates a conversion of wave kinetic energy into potential energy as heavy fluid is directed upward and light fluid is directed downward. In Figure 10, the negative peaks in $C(P,K')$ are slightly larger in magnitude than the adjacent positive peaks, whereas in simulation 1 (cf. Figure 6), where plume ejection was not observed, the negative peaks in $C(P,K')$ are smaller than the positive peaks.

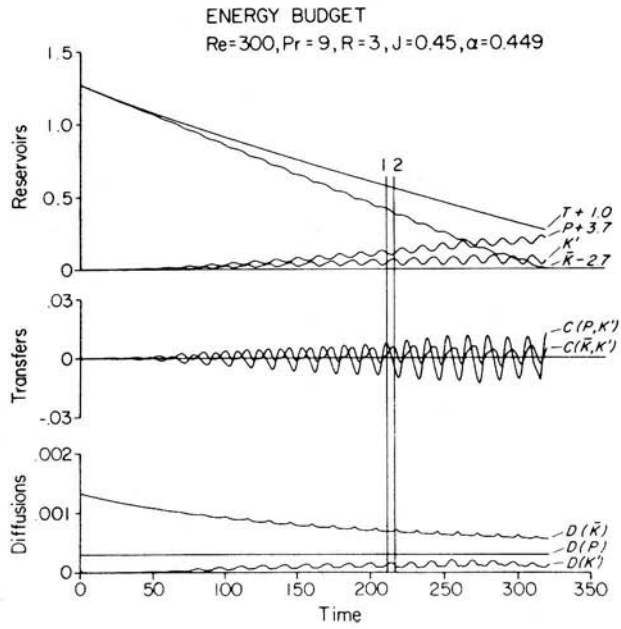

Figure 10 Energy budget for simulation 2. See Figure 6 for details.

While the value of $D(\bar{K})$ in simulation 1 becomes roughly constant (apart from periodic fluctuations) as the wave reaches maximum amplitude, it continues to decrease throughout the simulation at point 2. The fluctuations exhibited by $D(\bar{K})$ consist of very brief jumps which occur just as the component waves pass through the state of maximum separation. The value of $D(K')$, again ignoring periodic fluctuations, is very nearly equal to that found in simulation 1 for all times, although one might expect increased dissipation due to the greater degree of small-scale structure in the flow to be reflected in a generally larger value of $D(K')$.

The relative dominance of small scale structure in simulation 2 is apparent upon examination of the potential temperature field, which is shown along with the vorticity field in Figure 11. It will be observed that the vorticity fringes which appeared in simulation 1 due to underresolution are absent, as we have increased the number of grid points to 256×256 in order to resolve the small scale structures.

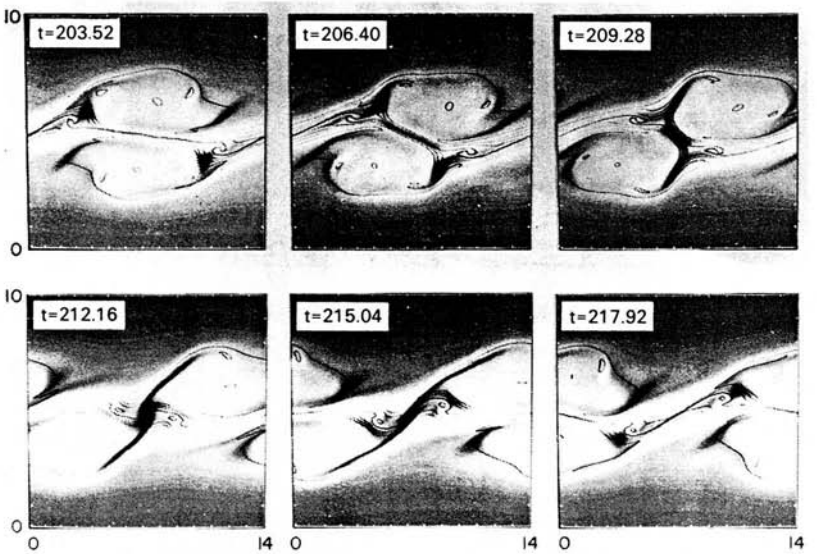

Figure 11 Potential temperature and vorticity for simulation 2. See Figure 7 for details.

In the inner regions of the component waves, near the central temperature interface, we see small regions of overturning fluid. At these points the potential temperature contours are spread apart, while vorticity is strongly concentrated. The local value of the gradient Richardson number is thus relatively small, which leads to overturning via Kelvin–Helmholtz instability.

In the lee of the component wave crests, concentrations of clockwise vorticity are clearly visible, and as the component waves approach each other, plumes develop which shed small parcels of fluid from their tips into the downstream vortices. We mentioned in Section 4.1 that plumes are generated when the vortices become strong enough to entrain stratified fluid from the downstream faces of the wave crests, and that this occurs primarily as the waves pass through the state of maximum separation and begin to approach each other. We now seek to explain why plume generation occurs at this particular point in the cycle.

The ability of a downstream vortex to entrain stratified fluid is controlled by two factors, namely the structure of the component wave and the strength of the vortex. The shape of one component of

the wave fluctuates due to nonlinear interactions with the second component. Fluctuations in the strength of the vortex, however, are to be expected as a consequence of changes in the phase speed of the component waves. As this phase speed fluctuates, so does the speed of the background flow in a reference frame moving with the wave, and the latter speed is the dominant factor which controls the strength of the downstream vortex. Results shown in Figure 5 reveal that when the component waves are widely separated, their phase speed is at a minimum, hence the strength of the downstream vortex is at a maximum. Conversely, the component waves move quickly as they pass each other, and the downstream vortices are thus relatively weak at this point. As a result, plumes grow as the waves approach each other and subside as they move apart.

We now examine the profiles of horizontally averaged velocity, potential temperature deviation, Reynolds stress and vertical heat flux shown in Figure 12, in which the six frames correspond to the six frames of the preceding figure. There is little variation in the potential temperature and velocity profiles through the half-cycle. The Reynolds stress profiles indicate a net flux of horizontal momentum into the centre of the shear layer as the component waves pass each other (frames 4 and 5) which is reversed as the waves move apart (frames 6 and 1). At the latter stage of the cycle, the heat flux profile shows a net flow of heat out of the centre of the shear layer which is reversed as the component waves approach each other (frames 3 and 4). These qualitative features are all similar to the results of simulation 1, shown in Figure 8.

In the later stages of wave evolution, illustrated in Figure 13, we see that the mean profiles of potential temperature and velocity have diffused considerably, and that vertical symmetry about the central level $z=H/2$ has been maintained, in contrast to the symmetry breaking observed in simulation 1 (Figure 9). As in Figure 9, the dashed curves on the $\bar{\theta}^*$ and $\bar{U}$ plots represent the initial conditions, while the dotted curves illustrate the diffusive mixing which would have occurred in the absence of wave growth. Comparing the vorticity field at $t=480$ with that shown in the third frame of Figure 11 (in which the wave exhibits the same configuration), we see that the vortices downstream of the component waves have weakened considerably. As an result there are no visible plumes, although it is apparent that the cumulative effect of plume entrain-

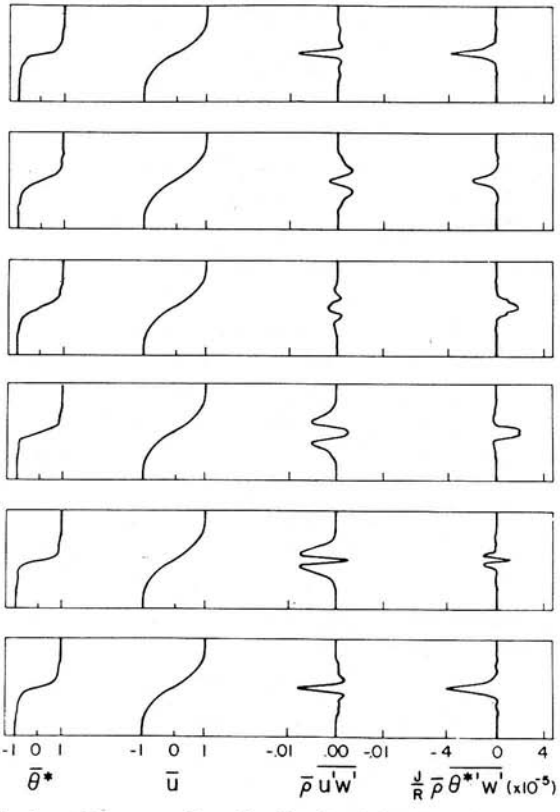

Figure 12 Horizontally averaged profiles for simulation 2 at times corresponding to Figure 11.

ment has led to substantial thermal mixing in the vortices. The momentum mixing which has occurred is due primarily to diffusion throughout the domain. This is in contrast with the results from the simulation of the more intensely stratified flow shown in Figure 9, where strong momentum mixing due to wave action is evident near the upper and lower edges of the domain. This contrast is probably due to the difference in linear growth rates between the two waves. The wave shown in Figure 9, having a relatively large growth rate, has attained an amplitude which is sufficient to influence the flow throughout the domain, whereas the more slowly growing disturbance shown in Figure 13 has remained confined to the vicinity of the shear layer.

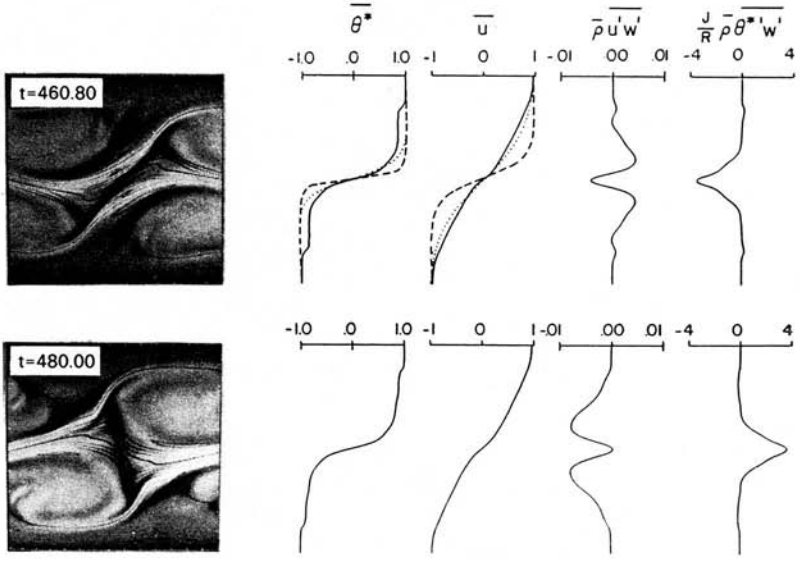

Figure 13 Late stages of simulation 2, as in Figure 9.

4.4 The time-dependent structure of a Kelvin–Helmholtz wave in a weakly stratified flow

We conclude this section of the paper with an examination of the data from the simulation at point 3 of Figure 2. In this case, small-scale structure developed to such an extent that, even using a 256×256 grid, the flow became underresolved shortly after the wave reached maximum amplitude. The energy budget is shown in Figure 14. The wave kinetic energy increases to a maximum near $t=80$. During this period the wave gains energy from the mean flow $[C(\bar{K}, K')>0]$, some of which is passed on to the potential energy reservoir $[C(P, K')<0]$. After $t=80$, K' decreases rapidly due to a large transfer of kinetic energy from the wave to the mean flow. During this period, the potential energy reservoir is also depleted as the vortex core of the Kelvin–Helmholtz wave flattens under the influence of gravity. In simulations of a Kelvin–Helmholtz wave in a flow with $R=1$ and $J=0.07$, Klaassen and Peltier (1985a) have shown that this three-way energy exchange (between $\bar{K}$ and P, via K') is quasi-periodic, i.e. that $C(\bar{K}, K')$ and $C(P, K')$ continue to exchange signs at regular intervals. The present simulation was not

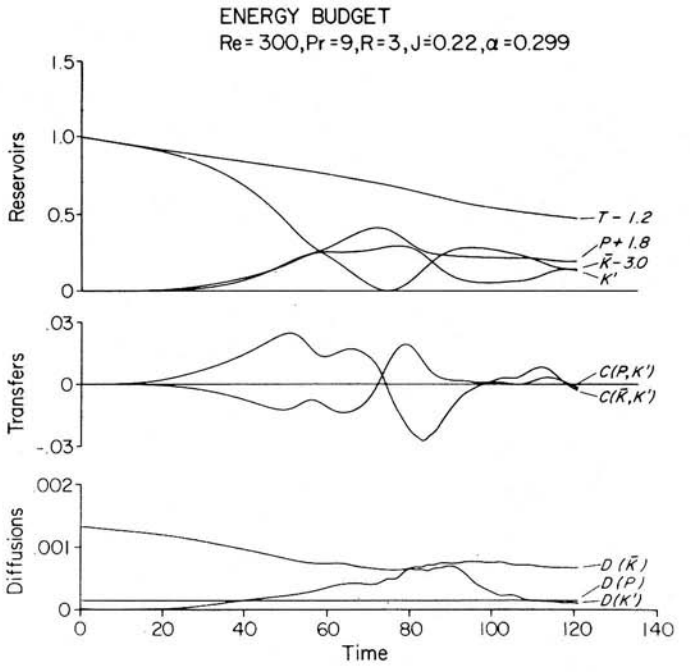

Figure 14 Energy budget for simulation 3.

extended for long enough to discover whether such periodicity would occur in this case.

The potential temperature and vorticity fields for simulation 3 are shown in Figure 15. It should be noted that while the Kelvin–Helmholtz vortex which forms appears round, it actually has a horizontal/vertical aspect ratio of about two, as the plots have been compressed by a factor of 2:1 in the horizontal direction. In the later stages of the simulation (not shown here), the aspect ratio of the vortex core increases to about four, then decreases again. A feature which was not observed in the simulations of Klaassen and Peltier (1985a) is the appearance of regions of clockwise vorticity in the core. This is due to baroclinic vorticity generation in the overturned regions, which is much more important in the present simulation than it was in the work of Klaassen and Peltier because of the more intense stratification employed in this instance.

In Figure 16 we see that the growth of the wave has a marked effect on the background profiles, particularly that of potential

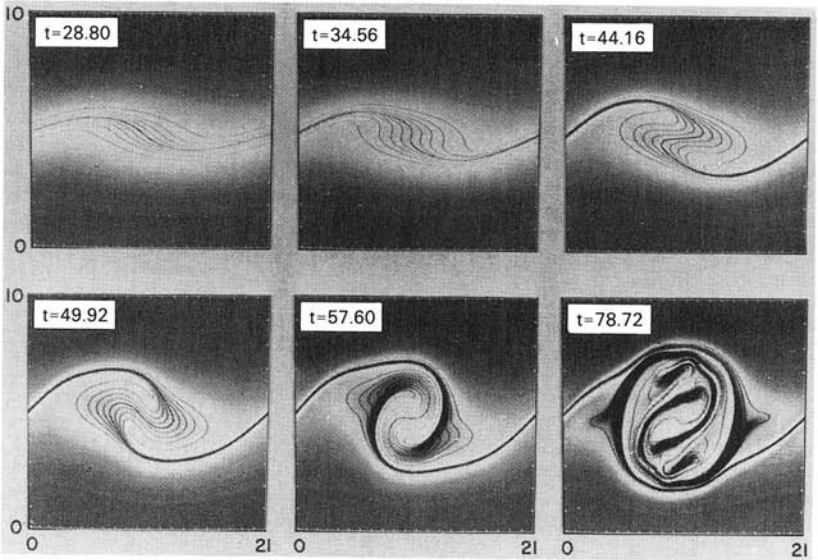

Figure 15 Potential temperature and vorticity for simulation 3. See Figure 7 for details.

temperature. Both thermal and momentum mixing in the Kelvin–Helmholtz simulation are due almost entirely to wave growth, since diffusion has not yet had time to modify the flow substantially. This is in contrast with the case of the more slowly growing Holmboe wave, whose contribution to the mixing of heat and momentum is comparable in magnitude to that of diffusion, as was seen in Figures 9 and 13. The Reynolds stress and heat flux due to the Kelvin–Helmholtz wave are both negative until the wave reaches maximum amplitude, at which point they become positive. This is in accord with the findings of Klaassen and Peltier (1985a).

5. SUMMARY

We have simulated the nonlinear evolution of an initially horizontal shear layer which contains at its centre a thin layer of stable density stratification. An inviscid linear stability analysis reveals that the flow is unstable, however strong the stratification may be. Kelvin–Helmholtz instability is predicted if the stratification is sufficiently weak; if the level of stratification exceeds a critical value, Holmboe instability appears.

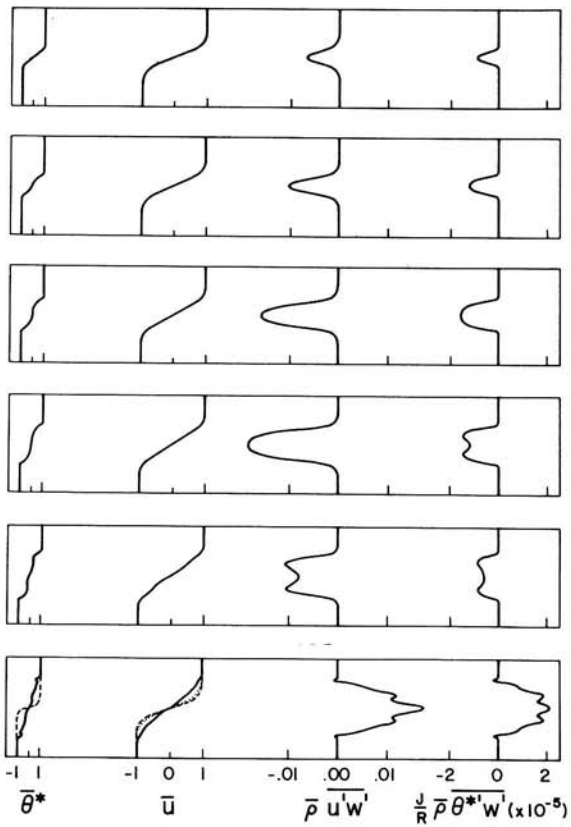

Figure 16 Horizontally averaged profiles for simulation 3 at times corresponding to Figure 15. As in Figure 9, the dashed and dotted curves in the final frame represent pofiles at $t=0$ and at the current time, evolving in the absence of wave growth.

While the behavior of Kelvin–Helmholtz waves has been described in detail in previous publications (e.g. Peltier *et al.*, 1978; Klaassen and Peltier, 1985a), the present study represents the first theoretical investigation of the nonlinear Holmboe wave. We have presented results from a sequence of three numerical simulations, employing strong, moderate, and weak stratification, by means of which the nonlinear evolution of the Holmboe wave and its relationship to the Kelvin–Helmholtz wave have been investigated.

The Holmboe wave consists of two horizontally propagating component waves, one propagating to the right and having its

largest amplitude in the upper (rightward moving) region of the shear layer, the other propagating to the left and residing primarily in the lower (leftward moving) region of the shear layer. The component waves resemble solitary waves in that they are highly localized in the horizontal direction. The lower component wave is inverted, i.e. its crest extends downward. Near the centre of the shear layer, the component waves have nearly equal amplitudes, and they thus interfere to create a standing oscillation.

The phase speeds of the upper and lower waves depend upon their relative position; they move quickly as they pass each other and more slowly when they are widely separated, with the phase speed reaching a minimum near the state of maximum separation. Downstream from the component waves, vortices form which are strongest when the component waves are moving slowly. During this phase (i.e. as the component waves approach each other), the vortices entrain long, thin plumes of stratified fluid from the downstream faces of the component waves, provided that the local stratification is not too strong. As the component waves pass each other and move apart again, the downstream vortices weaken and the plumes subside.

The average phase speed of the component waves decreases as the level of stratification is decreased, and since the waves are then able to interact more strongly, their tendency to decelerate when they are widely separated from each other increases. At some critical value of the bulk Richardson number, the minimum instantaneous phase speed of the component waves vanishes, this occurring near the state of maximum separation. The waves then become phase-locked in this configuration and wind around each other to form the Kelvin–Helmholtz vortex.

Holmboe waves in laboratory experiments are often observed to become three-dimensional very early in their evolution, and this, in combination with the fact that the linear growth rate of the Holmboe instability may increase with stratification, has prompted the suggestion that the primary Holmboe instability is three-dimensional (Lawrence *et al.*, 1987; also see Spedding, 1988). While this may be true for the low Reynolds number flows which occur in laboratory experiments, our analyses have indicated that when the Reynolds number is sufficiently large, the primary instability is two-dimensional, and we suggest that such flows become three-dimensional in consequence of a secondary instability. We intend to

test this conjecture in the near future by investigating the stability of two-dimensional Holmboe waves to infinitesimal three-dimensional perturbations by means of linear stability analysis, as was done for the nonlinear Kelvin–Helmholtz wave by Klaassen and Peltier (1985a). In addition, we are investigating the possibility that the fastest-growing primary Holmboe instability in a flow with sufficiently low Reynolds number is three-dimensional.* The results of these calculations will make possible the design of fully three-dimensional simulations of Holmboe waves, and will extend our current understanding of the transitions through which a stratified shear flow becomes turbulent.

*Recent computations have confirmed the existence, at low Reynolds number, of a region of parameter space in which the fastest-growing Holmboe instability is three-dimensional. The parameter values chosen for our simulations lie outside this region, but those which obtain in the laboratory experiments of Lawrence *et al.* 1987) may not. A detailed description of these results will be included in a subsequent publication.

Acknowledgements

The computations described in this paper were performed on the GRAY X-MP computer at Dorval Quebec that was made available through the Vector Computer Access program of the National Sciences and Engineering Research Council of Canada.

References

Batchelor, G. K., "The conditions for dynamical similarity of motions of a frictionless perfect-gas atmosphere," *Q. J. R. Meteorol. Soc.* **79,** 224 (1953).

Browand, F. K. and Wang, Y. H., "An experiment on the growth of small disturbances at the interface between two streams of different densities and velocities," *Proc. Int. Symposium on Stratified Flows,* August 29–31, 1972, Novosibirsk, Soviet Union (1972).

Browand, F. K. and Winant, C. D., "Laboratory observations of shear instability in a stratified fluid," *Boundary Layer Meteorol.* **5,** 67 (1973).

Busse, F., "Transition to turbulence in Rayleigh-Bénard convection," in *Hydrodynamic Instabilities and the Transition to Turbulence,* 2nd ed., (eds. H. L. Swinney and J. P. Gollub) Springer-Verlag (1981).

Clark, T. L., "A small-scale numerical model using a terrain following coordinate system," *J. Comput. Phys.* 24, 186 (1977).

Davis, P. A. and Peltier, W. R., "Resonant parallel shear instability in the stably stratified planetary boundary layer," *J. Atmos. Sci.* **33,** 1287 (1976).

Davis, P. A. and Peltier, W. R., "Some characteristics of the Kelvin–Helmholtz and resonant overreflection modes of shear flow instability and of their interaction through vortex pairing," *J. Atmos. Sci.* **36,** 2394 (1979).

Drazin, P. G. and Howard, L. N., "Hydrodynamic stability of parallel flow of inviscid fluid," *Adv. Appl. Mech.* **9,** 1 (1966).

Ellison, T. H. and Turner, J. S., "Turbulent entrainment in stratified flows," *J. Fluid Mech.* **6,** 423 (1959).

Emmanuel, C. B., Bean, B. R., McAllister, L. G. and Pollard, J. R., "Observations of Helmholtz waves in the lower atmosphere with an acoustic sounder," *J. Atmos. Sci.* **29,** 886 (1972).

Enright, W. H., Betet, R., Farkas, I. and Hull, T. E., "Test results on initial value methods for non-stiff ordinary differential equations," *University of Toronto Department of Computer Science, Technical Report* **No. 68** (1974).

Gossard. E. E. and Richter, J. H., "The shape of internal waves of finite amplitude from high-resolution radar sounding of the lower atmosphere", *J. Atmos. Sci.* **27,** 971 (1970).

Hazel, P., "Numerical studies of the stability of inviscid parallel shear flows," *J. Fluid Mech.* **51,** 39 (1972).

Holmboe, J., "On the behavior of symmetric waves in stratified shear layers," *Geophys. Publ.* **24,** 67 (1962).

Howard, L. N., "Note on a paper of John W. Miles," *J. Fluid Mech.* **10,** 509 (1961).

Keulegan, G. H., "Interfacial instabilities and mixing in stratified flows," *J. Res. Natl. Bur. Stand.* **43,** 487 (1949).

Klaassen, G. P. and Peltier, W. R., "The evolution of finite amplitude Kelvin–Helmholtz billows in two spatial dimensions," *J. Atms. Sci.* **42,** 1321 (1985a).

Klaassen, G. P. and Peltier, W. R., "The onset of turbulence in finite amplitude Kelvin–Helmholtz billows," *J. Fluid Mech.* **155,** 1 (1985b).

Klaassen, G. P. and Peltier, W. R., "The effect of Prandtl number on the evolution and stability of Kelvin–Helmholtz billows," *Geophys. & Astrophys. Fluid Dyn.* **32,** 23 (1985c).

Koop, C. G., "Instability and turbulence in a stratified shear layer," *Univ. Southern Calif., Dept. Aerospace Eng. Rep.* USCAE **134** (1976).

Koop, C. G. and Browand, F. K., "Instability and turbulence in a stratified layer with shear", *J. Fluid Mech.* **93,** 135 (1979).

Lawrence, G. A., Lasheras, J. C. and Browand, F. K., "Shear instabilities in stratified flow," Proc. 3rd. Int. Symposium on Stratified Flows, February 2–5, 1987, Pasadena, California (1987).

Maxworthy, T. and Browand, F. K., "Experiments in rotating and stratified flows: oceanographic applications," *Annu. Rev. Fluid Mech.* **7,** 273 (1975).

Miles, J. W., "On the stability of heterogeneous shear flows," *J. Fluid Mech.* **10,** 496 (1961).

Ogura, Y. and Phillips, N. A., "Scale analysis of deep and shallow convection in the atmosphere," *J. Atmos. Sci.* **19,** 173 (1962).

Peltier, W. R., Halle, J. and Clark, T. L., "The evolution of finite amplitude Kelvin–Helmholtz billows," *Geophys. & Astrophys., Fluid Dyn.* **10,** 53 (1978).

Peltier, W. R. and Clark, T. L., "The evolution and stability of finite-amplitude mountain waves. Part II: Surface wave drag and severe downslope windstorms," *J. Atmos. Sci.* **36,** 1498 (1979).

Ruelle, D. and Takens, F., "On the nature of turbulence," *Commun. Math. Phys.* **20,** 167; **23,** 343 (1971).

Spedding, G. R., "Dislocations and three-dimensional instabilities of Kelvin–Helmholtz waves," *Weather* **43,** (1), 25 (1988).

Squire, H. B., "On the stablity of three-dimensional disturbances of viscous flow between parallel walls," *Proc. R. Soc. London* A **142,** 621 (1933).

Thorpe, S. A., "A method of producing a shear flow in a stratified fluid," *J. Fluid Mech.* **6,** 693 (1968).

Thorpe, S. A., "On the shape of progressive internal waves," Philos. Trans. R. Soc. A **263,** 563 (1968).

Thorpe, S. A., "Transitional phenomena and the development of turbulence in stratified fluids: a review," *J. Geophys. Res.*, **92,** C5, 5231 (1987).

Townsend, A. A., "Turbulent flow in a stably stratified atmosphere," *J. Fluid Mech.* **3,** 361 (1958).

Tritton, D. J. and Davies, P. A., "Instabilities in geophysical fluid dynamics," in *Hydrodynamic Instabilities and the Transition to Turbulence*, 2nd ed. (eds. H. L. Swinney, J. P. Gollub) Springer-Verlag (1985).

Yih, C.-S., "Stability of two-dimensional parallel flows for three-dimensional disturbances," *Q. Appl. Math.* **12,** 434 (1955).

Yoshida, S., "On a mechanism for breaking of interfacial waves," *Coastal Eng. Japan* **20,** 7 (1977).

Appendix

STABILITY OF THE HOLMBOE MODEL TO TWO AND THREE-DIMENSIONAL DISTURBANCES

The piecewise-linear profiles shown by the dashed lines in Figure 1 provide a convenient model from which to predict the behavior of the more realistic flows which they approximate, because their stability properties can be investigated analytically. In this appendix, we seek to infer the dimensionality of the primary Holmboe instability in the general case by investigating the relevant stability characteristics of this simple model. The dispersion relation for the Holmboe profiles is

$$\sigma^4 + b\sigma^2 + c = 0, \tag{A.1}$$

in which (Holmboe, 1962; Drazin and Howard, 1964)

$$b = a_+ a_- + \alpha j, \quad c = \alpha j a_-^2,$$

$$j = \Delta g h / u_0^2, \quad a_\pm = (1 - 2\alpha \pm e^{-2\alpha})/2.$$

The contour plot of $\sigma(\alpha, j)$ is qualitatively very similar to that shown in Figure 2. It may be found in Browand and Wang (1972) or in Lawrence *et al.* (1987).

Our first objective is to define the curve $\alpha=\alpha_m(j)$ which is the locus of all points in the Holmboe wave regime at which the real part of σ is maximized with respect to α. The Holmboe wave regime is bounded by the curves on which the discriminant of (A.1), $(b+2c^{1/2})(b-2c^{1/2})$ vanishes. Differentiating (A.1) and setting $d\sigma$ to zero, we find

$$|\sigma|^4+\tfrac{1}{2}b|\sigma|^2+(dc/db)(\tfrac{1}{2}b+\sigma_r^2-3\sigma_i^2)=0. \tag{A.2}$$

Now since the roots σ^2 of (A.1) occur in complex conjugate pairs, we know that

$$2\sigma_r^2=c^{1/2}-\tfrac{1}{2}b; \quad 2\sigma_i^2=c^{1/2}+\tfrac{1}{2}b, \tag{A.3}$$

which enables us to eliminate σ from (A.2). The result may be rearranged to give

$$(b+2c^{1/2})(c^{1/2}-dc/db)=0. \tag{A.4}$$

The root $b+2c^{1/2}=0$ defines one boundary of the Holmboe wave regime. The other possibility, $c^{1/2}-dc/db=0$, may be integrated to give

$$c^{1/2}=\tfrac{1}{2}b+2\sigma_r^2, \tag{A.5}$$

where (A.3) has been used to identify the constant of integration. As we have assumed that the discriminant of (A.1) is negative, curves of constant σ_r are segments of parabolas in the (b, c) plane. When we rewrite (A.5) in terms of α and j, retaining the abbreviations a_+ and a_-, we find a quadratic equation for $(\alpha j)^{1/2}$ whose solutions are

$$(\alpha j)^{1/2}=|a_-|\pm(a_-^2-a_+a_--4\sigma_r^2)^{1/2}. \tag{A.6}$$

For a given value of α, the maximum possible growth rate is given by $\sigma_r^2=\frac{1}{4}a_-(a_--a_+)$, at which

$$(\alpha j)^{1/2}=|a_-|. \tag{A.7}$$

Equation (A.7) thus defines the curve on which the fastest-growing modes of instability are found.

We now examine these results to discover whether there is any point on the curve described by (A.7) at which the ratio σ_r^2/j increases with increasing j, the signal of a three-dimensional primary instability. The last two results combine with the definitions of a_+ and a_- to give

$$\sigma_r^2/j = \alpha(a_- - a_+)/4a_- = \tfrac{1}{2}\alpha e^{-2\alpha}/(e^{-2\alpha} + \alpha - 1), \tag{A.8}$$

the right-hand side of which is easily shown to be a monotonically decreasing function of α for all $\alpha > 0$. Since j increases monotonically with α on the curve defined by (A.7), σ_r^2/j increases monotonically with j. We thus conclude that the inequality (12) of Section 2 is not satisfied anywhere in the Holmboe wave regime, i.e. that the fastest-growing Holmboe mode in the piecewise-linear model is always two-dimensional.